A machine learning framework of ground-state properties of finite nuclei for accelerated Bayesian exploration : NucleiML*

Anagh Venneti[1] Chiranjib Mondal[2] Sk Md Adil Imam[3] Sarmistha Banik[1] Bijay K. Agrawal[4,5]

[1]Department of Physics, Birla Institute of Technology and Science, Pilani, Hyderabad Campus, Jawahar Nagar, Kapra Mandal, Medchal District, Telangana 500078, India
[2]Institut d'Astronomie et d'Astrophysique, Université Libre de Bruxelles, CP 226, B-1050 Brussels, Belgium
[3]Instituto de Astrofísica, Departamento de Física y Astronomía, Universidad Andrés Bello, Santiago, Chile
[4]Saha Institute of Nuclear Physics, 1/AF Bidhannagar, Kolkata, 700064, West Bengal, India
[5]Homi Bhabha National Institute, Anushakti Nagar, Mumbai, 400094, Maharashtra, India

Abstract: The overall behavior of the nuclear equation of state (EoS) is commonly studied using data from finite nuclei (FN), heavy-ion collisions, and astrophysical observations of neutron stars (NS). Constraints derived from FN, such as binding energies and charge radii, play a central role in shaping the EoS up to saturation density. The computational cost of explicitly incorporating these constraints presents a significant challenge, especially when the goal is to explore model uncertainties rather than optimize a single model. We address this challenge by introducing NucleiML (NML), a machine learning framework trained on ground-state properties of a selected set of finite nuclei generated by a relativistic mean-field model. NML enables efficient integration of FN and NS properties within a Bayesian inference framework. The results demonstrate reasonable accuracy and a speedup of $\sim 10^3$ for calculations of FN properties for a single parameter set and within the Bayesian framework. The present study supports extending this work to a larger set of nuclei, potentially enabling future studies of NS properties to incorporate the entire nuclear chart.

Keywords: Finite nuclei properties, ML based emulators, Charge Radius, Binding energy

DOI: 10.1088/1674-1137/aebcef **CSTR:**

CPC Accepted

I. INTRODUCTION

The equation of state (EoS) of dense baryonic matter plays a crucial role in determining the structural properties of neutron stars (NSs) and in understanding the density dependence of the nuclear symmetry energy [1, 2]. Nuclear EoSs are generally parameterized using empirical values of the binding energy per nucleon, the incompressibility coefficient of symmetric nuclear matter, and the symmetry energy coefficient, together with its slope at saturation density ($\rho_0 \simeq 0.16$ fm^{-3}). Usually, the impact of nuclear matter parameters (NMPs) on NS properties is examined by varying them independently within ranges determined by calibrating different mean-field models to experimental data on finite nuclei (FN). This calibration relies on measurements of binding energies [3], charge radii [4], isoscalar giant monopole resonances (ISGMR) [5], and other FN properties for different nuclei. Often, FN constraints are implicitly included in the analysis by imposing limits on the symmetry energy and symmetry pressure, as well as on the pressure of symmetric nuclear matter [6].

NS properties, such as mass, radius, and tidal deformability, have been inferred from pulsar observations [7, 8] and by the NICER [9−12] and LIGO-VIRGO-KAGRA [13] collaborations. These structural properties provide valuable insights into the internal composition of NSs and, consequently, into the behavior of highly asymmetric nuclear matter at high densities ($2–8\rho_0$). Heavy-ion collision (HIC) data, incorporated through the values of the nuclear symmetry energy and nuclear saturation properties [6, 14−16], constrain the behavior of nuclear matter at densities of $0.15–2\rho_0$. FN properties, such as binding energy [3], charge radius [4], and giant resonances [5], measured in nuclear physics experiments, are also crucial for understanding the properties of dense nuclear matter.

Recently [17], constraints on the binding energies and charge radii of ^{40}Ca and ^{208}Pb nuclei were explicitly incorporated alongside those from HICs and astrophysical observations of NS properties within a relativistic mean-field (RMF) model. This study highlights the crucial role

Received 10 April 2026; Accepted 2 November 2026

* AV acknowledges support from the CSIR-HRDG through CSIR-JRF 09/1026(16303)/2023-EMR-I. CM acknowledges partial support from the Fonds de la Recherche Scientifique (FNRS, Belgium) and the Research Foundation Flanders (FWO, Belgium) under EOS Project Nos. O022818F and O000422

©2027 Chinese Physical Society and the Institute of High Energy Physics of the Chinese Academy of Sciences and the Institute of Modern Physics of the Chinese Academy of Sciences and IOP Publishing Ltd. All rights, including for text and data mining, AI training, and similar technologies, are reserved.

of explicit FN constraints in understanding NS properties. The posterior distributions obtained in this study with explicit constraints revealed a distinct correlation pattern between the NMPs and NS properties, which differs from those inferred using implicit FN constraints [6]. The use of the RMF model [18−20] in the analysis introduces significant computational complexity, posing a challenge to extending the study to a diverse set of nuclei.

Machine learning (ML) methods have become indispensable in the modern data-driven scientific landscape, where exact models are often elusive. ML has also found widespread applications in fundamental physics research. In astrophysics, it has been used to identify signatures of various gravitational-wave signals from binary NS (BNS) mergers [21] and supernovae [22, 23], reconstruct gamma-ray burst (GRB) light curves [24, 25], recognize universal relations among neutron star properties [26, 27], detect potential dark matter signatures in neutron stars [28], and classify NS EoSs [29]. Owing to the complexity of nuclear and particle physics, ML holds significant promise for both theoretical modeling and experimental studies [30, 31]. In particular, ML techniques have received considerable attention in global nuclear mass models [32−35]. They have also been extensively used to derive suitable energy density functionals (EDFs) and develop nuclear models [34, 36−38]. Furthermore, ML-based statistical tests have been applied to nuclear models [39, 40], and ML methods have been used to infer the EoS of NS matter [41, 42]. The potential of ML tools in nuclear physics has been extensively reviewed in recent work [43−45]. Their growing importance, especially in nuclear astrophysics, has been emphasized, along with the need for caution when applying ML techniques to extrapolate beyond known data [46, 47].

Recent efforts to accelerate FN calculations have explored both reduced-order [48, 49] and data-analytic [50, 51] strategies. Projection-based approaches, such as reduced-basis methods [48, 49], have demonstrated substantial reductions in evaluation time for each parameter set. Simultaneously, data-driven surrogates [52] have been developed to approximate global nuclear observables and EDF predictions with substantial computational speedups. Although these advances have markedly reduced the cost of individual model evaluations, large-scale Bayesian analyses, which require millions of likelihood computations across multiple nuclei, still demand a framework that is both computationally efficient and easily retrained as datasets evolve. The computational cost of generating a training dataset is an offline cost incurred only once, whereas the cost of RMF evaluations is incurred repeatedly during Bayesian sampling. Therefore, a trained emulator can be reused for subsequent parameter-space explorations without repeating the RMF calculations or the training. The one-time computational cost is offset by the substantial savings achieved in subsequent large-scale Bayesian analyses. This motivates the adoption of artificial neural networks (ANNs), which are well suited to learning high-dimensional nonlinear mappings directly from data and can provide rapid evaluations without reformulating the underlying physics.

In this work, we introduce NucleiML (NML), a novel machine learning tool that incorporates a neural-network-based framework. The model is trained using a diverse dataset comprising various nuclei and their corresponding FN properties, derived from RMF-theory calculations for different NMPs. The performance of NML is evaluated by comparing its predictions with RMF model computations for both nuclei included in the training set and those not encountered during training. NML is also integrated into a Bayesian inference framework, where the resulting posterior distributions exhibit remarkable agreement with those obtained from an analogous analysis using the RMF model [18−20].

The present paper is structured as follows. Section II provides a brief overview of the RMF formalism employed to construct the training data for NucleiML. Section III describes the architecture, training, and evaluation of NML. In Section IV, NML is applied to a Bayesian analysis, and the resulting posteriors are compared with those obtained using the RMF model. Finally, Section V presents the summary and outlook.

II. RELATIVISTIC MEAN FIELD MODEL

We use the relativistic mean-field (RMF) model [53−55] to calculate properties, such as the binding energy and charge radius, for a given nucleus $^{A}\mathrm{X}_{Z}$. In an RMF model, nuclear matter is described by a Lagrangian in which nucleons interact through the exchange of attractive short-range σ mesons, repulsive very-short-range ω mesons, and ρ mesons that mediate isospin-dependent interactions. In addition to mediating these interactions, the mesons also exhibit self-interactions (for the σ and ω mesons) and cross-interactions (between the ω and ρ mesons). The Lagrangian is defined as follows:

$$\mathcal{L}_{NL} = \mathcal{L}_{nm} + \mathcal{L}_{\sigma} + \mathcal{L}_{\omega} + \mathcal{L}_{\rho} + \mathcal{L}_{int}, \tag{1}$$

where,

$$\begin{aligned}
\mathcal{L}_{nm} &= \bar{\psi}\left(i\gamma^{\mu}\partial_{\mu} - m\right)\psi + g_{\sigma}\sigma\bar{\psi}\psi - g_{\omega}\bar{\psi}\gamma^{\mu}\omega_{\mu}\psi - \frac{g_{\rho}}{2}\bar{\psi}\gamma^{\mu}\vec{\rho}_{\mu}\vec{\tau}\psi, \\
\mathcal{L}_{\sigma} &= \frac{1}{2}\left(\partial^{\mu}\sigma\partial_{\mu}\sigma - m_{\sigma}^{2}\sigma^{2}\right) - \frac{A}{3}\sigma^{3} - \frac{B}{4}\sigma^{4}, \\
\mathcal{L}_{\omega} &= -\frac{1}{4}\Omega^{\mu\nu}\Omega_{\mu\nu} + \frac{1}{2}m_{\omega}^{2}\omega^{\mu}\omega_{\mu} + \frac{C}{4}\left(g_{\omega}^{2}\omega_{\mu}\omega^{\mu}\right)^{2}, \\
\mathcal{L}_{\rho} &= -\frac{1}{4}\vec{B}^{\mu\nu}\vec{B}_{\mu\nu} + \frac{1}{2}m_{\rho}^{2}\vec{\rho}_{\mu}\vec{\rho}^{\mu}, \\
\mathcal{L}_{int} &= \frac{1}{2}\Lambda_{v}g_{\omega}^{2}g_{\rho}^{2}\omega_{\mu}\omega^{\mu}\vec{\rho}_{\mu}\vec{\rho}^{\mu}.
\end{aligned} \tag{2}$$

CPC Accepted

Here, $\Omega_{\mu\nu} = \partial_\nu\omega_\mu - \partial_\mu\omega_\nu$ and $\vec{B}_{\mu\nu} = \partial_\nu\vec{\rho}_\mu - \partial_\mu\vec{\rho}_\nu - g_\rho\left(\vec{\rho}_\mu \times \vec{\rho}_\nu\right)$. The masses of the nucleon and the σ, ω, and ρ mesons are denoted by m, $m_\sigma = 508.1941$, $m_\omega = 782.501$, and $m_\rho = 763.00$, respectively. Nuclear matter parameters (NMPs), including the energy per particle of symmetric matter E_0, isoscalar incompressibility K_0, isoscalar skewness Q_0, Dirac effective mass of nucleons m^*/m, symmetry energy J_0, and symmetry slope parameter L_0, all evaluated at saturation density ρ_0, determine the coupling parameters g_σ, g_ω, A, B, C, g_ρ, and Λ_v [53, 54]. The ranges of the NMPs used in this study are listed in Table 1.

The computational algorithm for determining the FN properties, given a set of nuclear matter parameters (NMPs) and a specific spherical nucleus ${}^A\mathrm{X}_Z$, can be outlined within the framework of RMF theory as follows [18−20]:

- The NMPs are used to determine the coupling parameters in the Lagrangian (Eq. 1), from which the field equations for mesons, photons, and nucleons are derived.

- These field equations are then solved by expanding the nucleon and meson fields in a harmonic-oscillator basis, yielding the basis occupation numbers, n_i, along with the corresponding meson- and spinor-field values.

- The resulting field values and occupation numbers, n_i, are then used to compute the binding energy and charge radius.

III. NUCLEIML

A. The algorithm

Statistical methods, such as Bayesian analyses, rely on random sampling of parameters and repeated model evaluations. As the number of evaluations increases, computational costs rise substantially, making it challenging to incorporate explicit FN constraints [17] together with those from heavy-ion collisions [6, 14−16, 56−58] and astrophysical observations [7, 9−13] in large-scale sampling. Machine learning techniques, particularly neural networks, provide an effective approach for improving computational efficiency while emulating RMF-model predictions. A precomputed set of RMF calculations provides predictions only at the sampled points in the underlying parameter space, whereas Bayesian sampling requires evaluations at arbitrary combinations of the NMPs within the adopted prior domain.

Table 1. Ranges of NMPs used to compute the properties of finite, closed-shell spherical nuclei within RMF theory

Parameters	Values	Units
ρ_0	0.14 - 0.17	fm^{-3}
E_0	−16.5 - -15.5	MeV
K_0	150 - 300	MeV
Q_0	−1500 - 400	MeV
m^*/m	0.5 - 0.8	–
J_0	20 - 40	MeV
L_0	20 - 100	MeV

NucleiML (NML) is a neural network-based framework designed to emulate the predictions of the RMF model while improving computational speed and maintaining close agreement with the underlying model. As illustrated in Fig. 1, the NML algorithm follows a two-step implementation process. First, an input set of NMPs and a nucleus ${}^A\mathrm{X}_Z$ are classified into one of two categories: *admissible* and *non-admissible*. These classes are determined from the behavior of the inputs. The *admissible* class comprises inputs determined to yield convergent results for finite nuclear properties. The *non-admissible* inputs are those that do not yield a valid set of coupling parameters, convergent FN properties, or FN properties within 20% of the experimentally determined values.

In the second step, a neural network regressor is employed to calculate the predicted binding energies and charge radii of ${}^A\mathrm{X}_Z$ for inputs classified as *admissible* by the NML classifier. The neural networks are built and trained using the Python packages *Tensorflow*[59] and *Keras*[60].

A crucial step in optimizing neural network performance is hyperparameter estimation. This is performed through a grid search to optimize the number of layers, the number of neurons per layer, and the number of training epochs. For this purpose, we use the Sklearn and SciKeras packages[61] to identify the optimal hyperparameter configuration that minimizes loss while maximizing accuracy by iterating over a grid of all possible hyperparameter values.

Different hyperparameter settings are typically employed to capture the diverse patterns of the underlying model. In this study, we primarily vary three hyperparameters while keeping the others fixed. The number of training epochs is selected to balance efficiency and accuracy, preventing both underfitting due to too few epochs and overfitting due to an excessively large number. The depth of the network (number of layers) and the number of neurons per layer are selected to capture the required model complexity and data variability while controlling computational cost. The learning rate controls the speed and stability of weight optimization during training. Table 2 summarizes the hyperparameters determined by the grid search for the NML classifier and regressor. Further discussion of the significance of other hyperparameters and additional hardware specifications are provided in A.

CPC Accepted

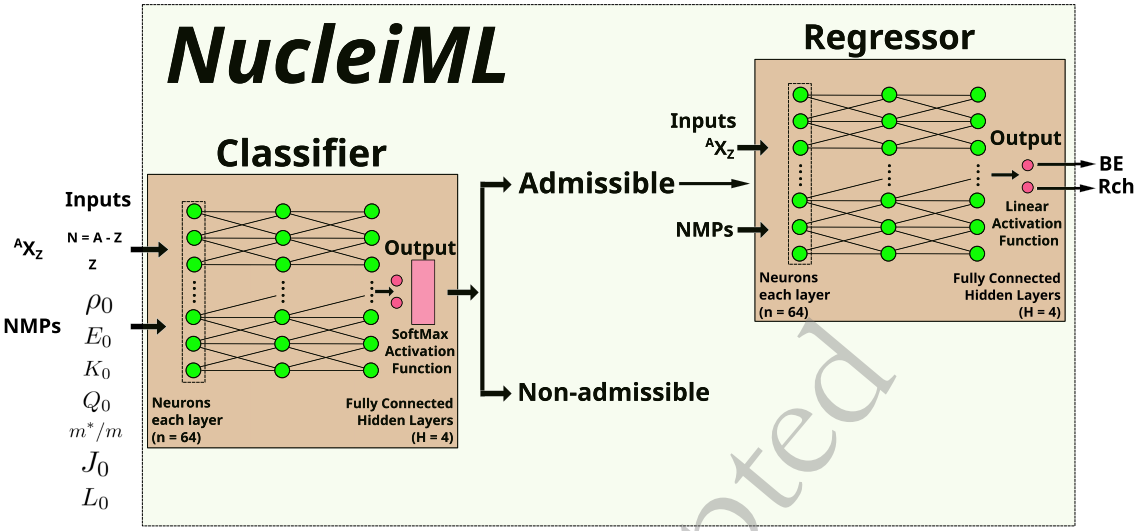


Fig. 1. (color online) Schematic representation of NucleiML (NML), detailing its classifier and regressor. Details of the activation functions and architecture are provided in Table 2 and A.

Table 2. The neural network hyperparameters were estimated using a grid search that minimized the loss and thereby maximized the neural network's accuracy.

NN Model	Epochs	Layers	Neurons	learning rate
NML Classifier	800	4	64	0.0001
NML regressor	500	4	64	0.001

B. The Classifier

1. *Training*

We construct a large data set by randomly sampling the seven NMPs; these samples are then used to determine the seven coupling constants of the Lagrangian in Eq. 1. These coupling parameters serve as inputs for computing the ground-state properties of five spherically symmetric closed-shell nuclei: $^{16}O_8$, $^{40}Ca_{20}$, $^{48}Ca_{20}$, $^{132}Sn_{50}$, and $^{208}Pb_{82}$, within the RMF model. The data set includes the NMPs, coupling parameters, corresponding binding energy (BE), charge radius (R_{ch}), and class (whether *admissible* or *non-admissible*) of a nucleus, $^{A}X_{Z}$. The NMPs, together with the nucleus identifiers N and Z, serve as inputs to both the classifier and the regressor. The classifier maps these inputs to a class label (admissible or non-admissible), whereas the regressor maps them to the corresponding FN observables.

Before being input into the NML classifier, the inputs, namely the NMPs and nucleus $^{A}X_{Z}$, are scaled and normalized. This step ensures that widely varying parameter values do not unduly influence the neural-network training process. The data set is then divided into three subsets: training, validation, and testing sets, using a 70%–15%–15% split, respectively. The classifier is trained to minimize categorical cross-entropy and learn diverse classification trends from the training data set. The categorical cross-entropy loss function [62] is defined as

$$H = -\sum_{i} p_i \times log(q_i), \tag{3}$$

where p_i and q_i are the components of the true and predicted class-probability vectors, respectively. During each training epoch, the neural network is first trained on the training set and then evaluated on the validation set to assess its ability to generalize to unseen data.

As illustrated in Fig. 2, the training loss of the NML classifier is initially high and decreases gradually as training progresses, eventually stabilizing at ~ 0.2. The validation loss exhibits minor fluctuations but follows a similar downward trend. This behavior suggests that the NML classifier generalizes effectively to unseen data. Moreover, the absence of a substantial divergence between the training and validation losses indicates that the model does not overfit the training data. The accuracy trends for both the training and validation sets further support this observation. Across successive epochs, the accuracy increases steadily and stabilizes at approximately 95%, demonstrating the effectiveness of the classifier in distinguishing between the categories.

The classifier serves as a computationally efficient surrogate for physical admissibility, helping to restrict Bayesian sampling to numerically stable and phenomenologically meaningful regions of parameter space. A detailed discussion of the motivation, representative examples of non-admissible parameter sets, sensitivity to threshold choices, and quantitative impact on posterior inference is presented in B.

CPC Accepted

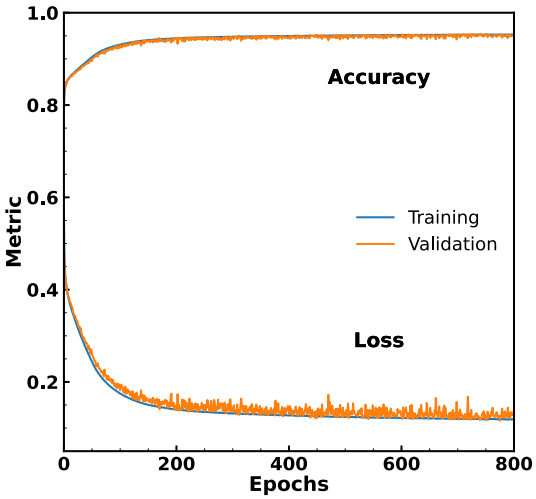


Fig. 2. (color online) The classifier's training loss and accuracy across training epochs. The training loss progressively decreases before stabilizing at approximately 0.2. The accuracy also improves progressively, stabilizing at ~ 0.95.

2. *Performance*

We evaluated the performance of the NML classifier using accuracy, precision, recall, and the F1 score. These metrics are defined as follows:

$$\text{Precision} = \frac{TP}{TP+FP}, \tag{4}$$

$$\text{Recall} = \frac{TP}{TP+FN}, \tag{5}$$

$$F_1 = 2\frac{\text{Precision}\times\text{Recall}}{\text{Precision}+\text{Recall}}, \tag{6}$$

where TP, FP, and FN denote the true-positive, false-positive, and false-negative counts, respectively, for the class under consideration. The classifier achieves an overall accuracy of 95%, demonstrating its effectiveness in categorizing inputs, consistent with observations during neural network training (Fig. 2). Additional metrics, such as precision and recall, provide deeper insight into classifier performance across classes. Precision measures the proportion of correctly predicted instances for a given class among all instances predicted to belong to that class. Recall quantifies the proportion of correctly classified instances among all actual instances of a particular class. The F1 score, the harmonic mean of precision and recall, is particularly useful for imbalanced datasets because it provides a more balanced assessment of classification performance. Table 3 summarizes these metrics. The NML classifier achieves an overall test accuracy of 95%, with precision, recall, and F1 scores of approximately 0.93–0.97 across the two classes. The strong precision and recall scores for both classes further demonstrate the classifier's ability to capture class-wise diversity in the data.

Fig. 3 presents the confusion matrix, illustrating the true and predicted labels. The diagonal elements represent correctly classified instances, with larger values indicating better classification performance. Misclassifications are shown in the off-diagonal elements. The test data set size (~ 150,000) can be obtained by summing all instances shown in the confusion matrix. As detailed previously in Table 3, the NML classifier exhibits strong performance across the two classes, as evidenced by the high values of the diagonal elements. The classifier is particularly valuable for controlling the acceptance rate when sampling from a Bayesian posterior distribution,

Table 3. Performance metrics for the classifier evaluated on the test dataset. The complete dataset contains approximately 1,000,000 samples and is divided into training, validation, and test sets (see Appendix A). The reported accuracy, precision, recall, and F1 score are evaluated exclusively on the test set.

Class	Precision	Recall	F1 Score
Admissible	0.93	0.97	0.95
Non admissible	0.97	0.94	0.95
Total Accuracy			0.95

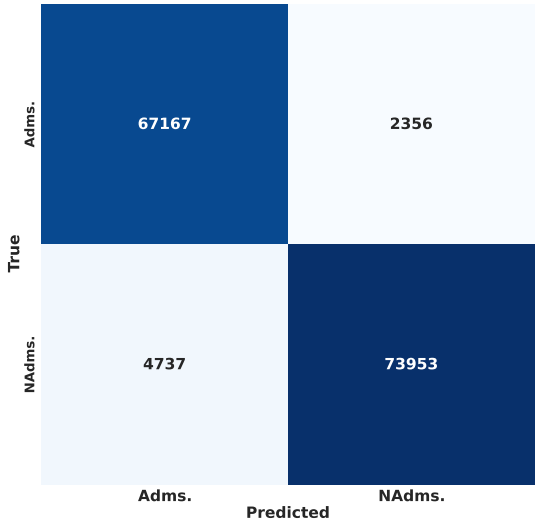


Fig. 3. (color online) The true and predicted labels are presented in a confusion matrix. The diagonal elements represent correctly classified instances, whereas the off-diagonal elements indicate misclassifications. Larger values along the diagonal, indicated by darker shades of blue, suggest strong classifier performance and provide insight into class-wise accuracy. Adms. and NAdms. denote the classes *Admissible* and *Non-admissible*.

CPC Accepted

thereby minimizing the risk of sampling outliers in the data.

C. The Regressor

1. *Training*

The second component of the NML framework is the regressor. The calculation of FN properties, such as binding energy and charge radius, for a given set of NMPs and a nucleus ${}^{A}\mathrm{X}_{Z}$ is formulated as a regression problem. As with the classifier, the inputs to the regressor are scaled and normalized. The outputs, however, are left unscaled because scaling does not significantly affect the predictive performance of the regressor. For the regressor, we used a 70%–21%–9% split of the dataset for training, validation, and testing, respectively. The neural network is trained to capture the underlying trends in the training dataset by minimizing a loss function. Specifically, we use the mean absolute percentage error (MAPE) [63] as the loss function, defined as follows:

$$MAPE = 100\frac{1}{n}\sum_{t=1}^{n}\left|\frac{A_t - P_t}{A_t}\right|, \tag{7}$$

where A_t and P_t are the actual and predicted values, respectively, and n is the total number of training data points. The performance of the regressor is quantified using the R^2 score, defined as

$$R^2 = 1 - \frac{\sum_i (y_i - \hat{y}_i)^2}{\sum_i (y_i - \bar{y})^2}. \tag{8}$$

Fig. 4 shows that the training loss decreases steadily over epochs for both binding energy and charge radius, converging to ~ 0.6%. The initial fluctuations in validation loss are due to randomly initialized weights during the early stages of training. Stochastic mini-batch training and learning-rate dynamics in a non-convex loss space contribute to the remaining variability. Nevertheless, the overall trend shows a steady reduction in loss, followed by stabilization as the number of epochs increases. The regressor achieves a global R^2 score of 0.998, computed across the complete test dataset by aggregating predictions for all nuclei and both observables. This result indicates that NML faithfully reproduces the overall variance structure of the aggregated dataset.

2. *Performance*

In Fig. 5, we present the probability density distributions of the relative deviations between the predicted and true values of the binding energy and charge radius of FN. The corresponding means and standard deviations

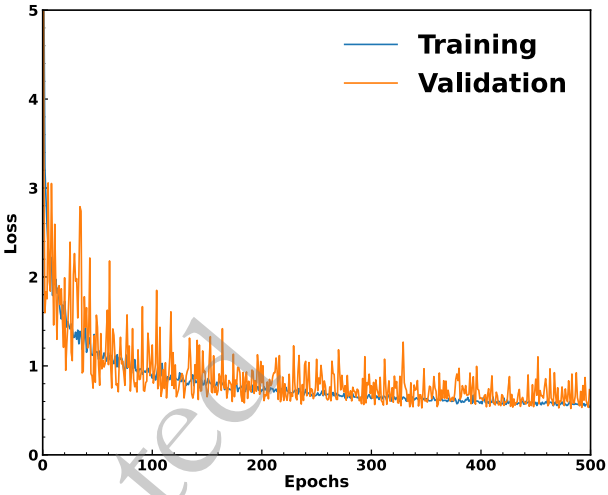


Fig. 4. (color online) The training of the regression model for binding energy and charge radius is shown. The mean absolute percentage error (MAPE) loss decreases as neural-network training proceeds over more epochs. The training and validation losses exhibit similar trends, with progressive improvement and the training loss stabilizing at ~ 0.6%.

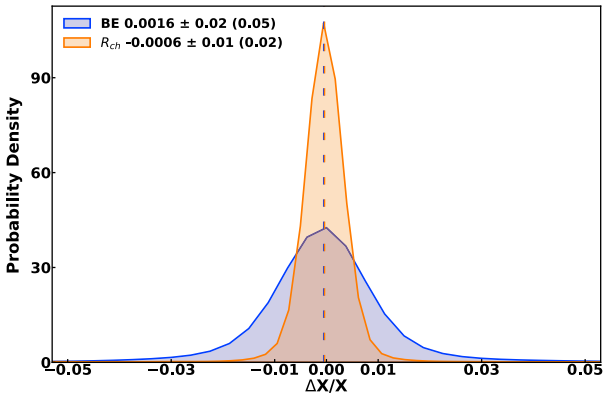


Fig. 5. (color online) Kernel-density estimates of the individual percentage deviations $\Delta X/X$ for the nuclei used in training, evaluated on the test dataset of NMPs, for binding energy (BE) and charge radius (R_{ch}). The mean and standard deviation of the individual deviations are shown in the legend, with the corresponding 95% confidence intervals reported in parentheses.

are reported in the legend. The deviation $\Delta X/X$ is defined as,

$$\frac{\Delta X}{X} = \frac{X_{true} - X_{pred}}{X_{true}} \tag{9}$$

where X represents either the binding energy or the charge radius. The deviations for the FN properties peak around zero and exhibit reasonably narrow distributions, indicating the accuracy of the NML regressor. The distributions appear approximately Gaussian, with the mean

CPC Accepted

(μ) centered near zero and the spread characterized by the standard deviation (σ). The binding energy shows a broader distribution ($\sigma \sim 0.05$) than the charge radius ($\sigma \sim 0.02$), as also reflected in the σ and 2σ intervals.

We analyze the performance of the NML regressors for selected nuclei, such as $^{40}Ca_{20}$ and $^{208}Pb_{82}$, in Fig. 6. We present joint distributions (blue for binding energy and red for charge radius) that illustrate the distribution of FN properties computed using the RMF model alongside the corresponding NML predictions. The experimentally determined values are represented by vertical and horizontal black dotted lines, while the dashed black line indicates the ideal regression line. The per-nucleus R^2 score for each observable is also reported. Fig. 6 also shows the marginalized 1D posterior distributions of the FN properties obtained from the RMF and NML models, along with the Jensen-Shannon (JS) divergence[64], which is defined as

$$JS(P \parallel Q) = \frac{1}{2} KL(P \parallel M) + \frac{1}{2} KL(Q \parallel M), \tag{10}$$

where

$$M = \frac{1}{2}(P + Q), \tag{11}$$

where P and Q are the distributions of RMF and NML

CPC Accepted

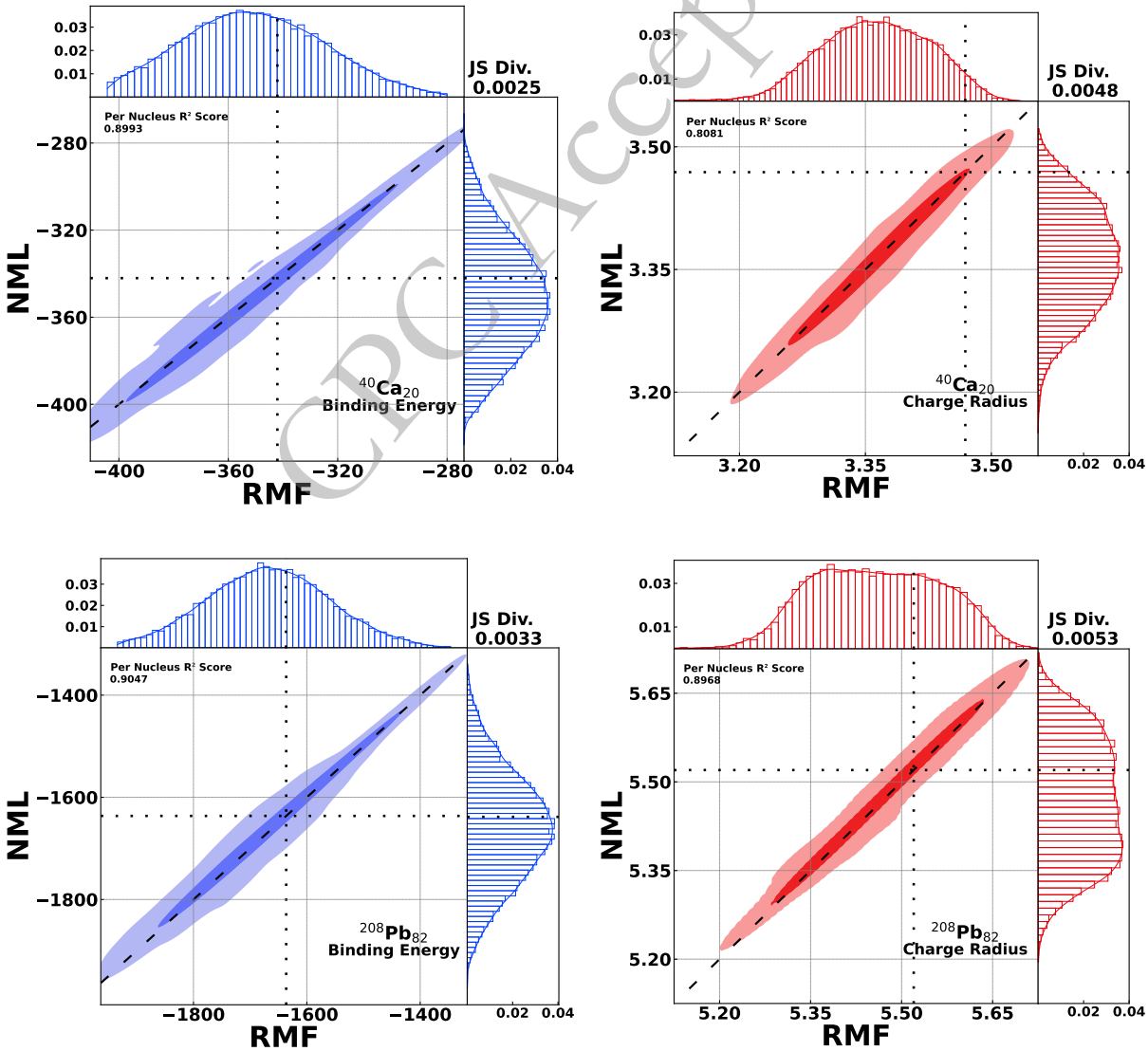


Fig. 6. (color online) Kernel density estimate (KDE) distributions are shown for the predictions of the binding energy and charge radius of $^{40}Ca_{20}$ and $^{208}Pb_{82}$ from the RMF model and NucleiML. The experimental values are indicated by vertical and horizontal black dotted lines. The ideal regression line is shown as a black dashed line. In addition, the marginalized distributions from both models and the JS divergence values between them are displayed. The per-nucleus R^2 score for each observable is also indicated.

predictions, respectively. $KL(A||B)$ denotes the Kullback–Leibler (KL) divergence [65, 66] between two distributions and quantifies their difference.

NML effectively predicts the FN properties and closely follows the ideal regression trend. The per-nucleus R^2 scores validate this agreement, with the highest value (~ 0.91) for the binding energy of $^{208}Pb_{82}$ and the lowest (~ 0.81) for the charge radius of $^{40}Ca_{20}$. This indicates that the model reasonably approximates RMF predictions while exhibiting greater variability at the individual-nucleus level than is reflected in the aggregated global performance indicated by the high global R^2 score. The JS divergence values further demonstrate strong similarity between the distributions obtained from NML and the RMF model. This complements the pointwise regression metrics by establishing distribution-level agreement with the underlying model. A detailed nucleus-wise breakdown of the predictive performance is provided in C.

Fig. 7 presents the performance of the NML regressor by showing the probability distribution of the deviation $\Delta X/X$ for (a) binding energy and (b) charge radius in nuclei that were not included in the training set. For the untrained set, we consider seven nuclei: $^{30}Ne_{10}$, $^{54}Ca_{20}$, $^{56}Ni_{28}$, $^{100}Sn_{50}$, $^{116}Sn_{50}$, $^{138}Sn_{50}$, and $^{144}Sm_{62}$. As shown, the initial training set, consisting of five selected spherically symmetric closed-shell nuclei, $^{16}O_8$, $^{40}Ca_{20}$, $^{48}Ca_{20}$, $^{132}Sn_{50}$, and $^{208}Pb_{82}$, exhibits a broad deviation distribution (shown in blue). This suggests difficulty in accurately predicting the properties of unseen nuclei and highlights the need for a more diverse training dataset. To address this limitation, we expand the training set by incorporating additional nuclei in multiple stages. First, we introduce three neutron-rich nuclei, $^{24}O_8$, $^{58}Ca_{20}$, and $^{78}Ni_{28}$, and retrain the model. The resulting deviation distribution (shown in orange) indicates an improvement, with the median deviation shifting closer to zero and the overall spread becoming narrower. Further improvements are observed when two additional nuclei, $^{68}Ni_{28}$ and $^{90}Zr_{40}$, are included in the training set. The median deviation moves even closer to zero, and the distribution (shown in green) tightens significantly, demonstrating improved accuracy. A quantitative comparison of per-nucleus R^2 scores for the initial and extended training sets shows a substantial improvement in performance. Several nuclei show noticeable gains after inclusion of the extended set compared with the initial configuration (see C for further details). These results underscore the importance of training on a more diverse range of nuclei to improve the predictive performance of the NML regressor.

D. Accuracy of NML

A deviation of 5% provides a reasonable starting point for the objective of developing a computationally efficient emulator of explicit finite-nuclei constraints. Among the ~ 120,000 sampled input parameter sets, only about 4000 (~ 4%) exceed this deviation, indicating that NML struggles only for a small fraction of inputs. Further examination of these parameters shows that their distribution differs from that of the remaining parameters, for which NML performs reliably.

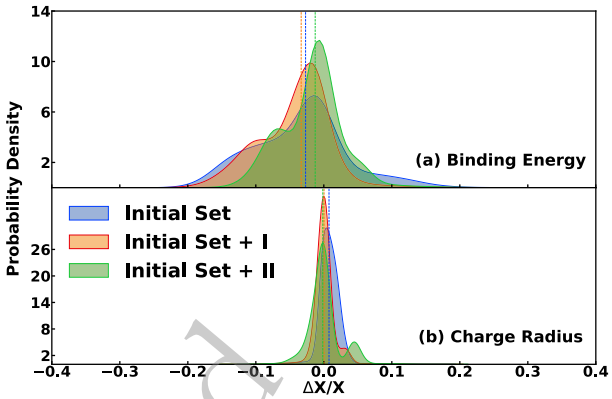


Fig. 7. (color online) Kernel-density estimates of the individual percentage deviations $\Delta X/X$ in (a) binding energy and (b) charge radius for nuclei not included in the regressor training set. The nuclei used for training are color-coded, with blue denoting the initial set of nuclei ($^{16}O_8$, $^{40}Ca_{20}$, $^{48}Ca_{20}$, $^{132}Sn_{50}$, and $^{208}Pb_{82}$). Orange and green denote training sets I ($^{24}O_8$, $^{58}Ca_{20}$, and $^{78}Ni_{28}$) and II ($^{24}O_8$, $^{58}Ca_{20}$, $^{78}Ni_{28}$, and $^{68}Ni_{28}$, along with $^{90}Zr_{40}$), respectively, in addition to the nuclei initially considered for training.

A comparison with the experimental data sheds further light on this behavior. For samples in which NML deviates from RMF by more than 5%, the RMF predictions themselves exhibit a median deviation of ~ 8% from the experimental binding energies. Conversely, for samples in which RMF deviates from experiment by less than 2%, NML reproduces the RMF predictions to within about 2%. This indicates that the largest deviations of NML occur mainly for outliers, where RMF predictions are already less reliable, while NML closely reproduces RMF results for well-behaved cases.

Although errors of ~2% appear large compared with global mass models that target keV-scale accuracy, they are acceptable for our objective of reducing the computational cost of incorporating explicit finite-nuclei constraints in the study of the NS EoS. A 5% deviation is therefore used here as a practical diagnostic threshold for identifying the small fraction of less accurate predictions. The suitability of the emulator for the Bayesian application is assessed separately through the agreement of the NML- and RMF-based posteriors. In addition, experimental values of charge radii are incorporated into the explicit finite-nuclei constraints, where the reliability of NML in reproducing the charge radii of different nuclei (<1%) helps compensate for the larger uncertainty in binding energies.

For Bayesian applications, the relevant accuracy cri-

CPC Accepted

terion is application-dependent and should be assessed relative to the uncertainty scale entering the likelihood. In particular, the emulator error should be sufficiently smaller than the adopted likelihood uncertainty so that replacing the underlying RMF calculation with NML does not materially change the posterior. In the present study, the agreement between the NML- and RMF-based posterior distributions in Fig. 8 provides a direct validation of this requirement for the adopted Bayesian setup.

IV. A SAMPLE BAYESIAN RUN

The primary objective of this work is to employ NML as a computationally efficient alternative to RMF predictions of finite-nuclei properties, enabling their explicit inclusion in Bayesian analyses of neutron-star equations of state. Previous studies [1, 2, 17] have shown that low-density constraints from finite nuclei strongly influence neutron-star properties and their correlations with NMPs. However, the high computational cost of mean-field calculations prevents such constraints from being systematically applied. In this study, we demonstrate the feasibility of using NML in a Bayesian analysis, emphasizing its ability to reproduce the predictions of its underlying microscopic model, RMF. This work is intended as a first step toward a broader program that incorporates both ground-state and excitation properties of nuclei in the context of nuclear astrophysics.

CTC Accepted

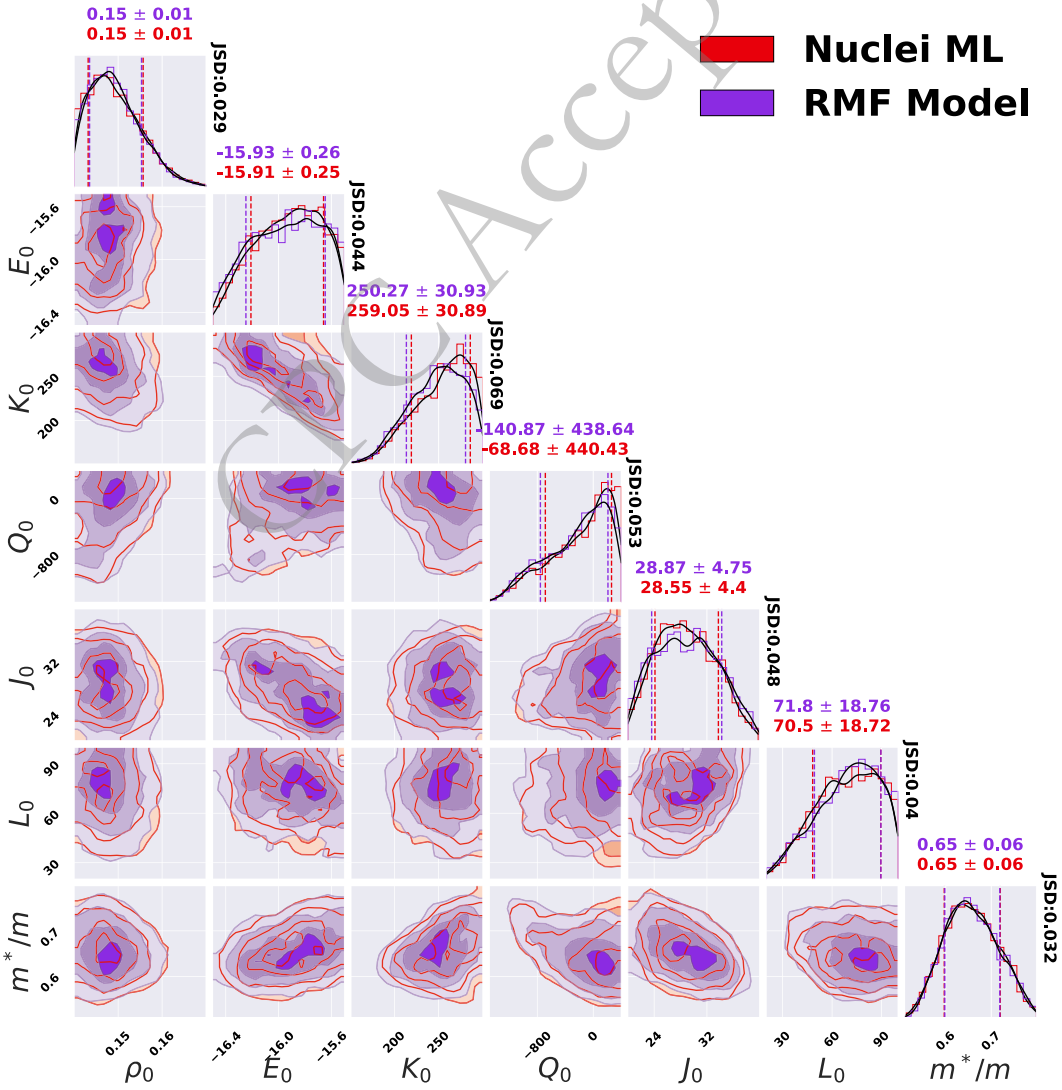


Fig. 8. (color online) The posterior distributions from the Bayesian analyses using the NML and RMF models are presented. The median values for both cases are shown above the diagonal plots, which also display the marginalized posterior distributions, with the 68% CI indicated by vertical dashed lines. The Jensen-Shannon divergence (JSD), which quantifies the difference between the parameter distributions in the two cases, is shown vertically alongside the marginalized posteriors. The smooth curves in the diagonal panels show kernel-density estimates of the corresponding one-dimensional marginalized posterior distributions, obtained using KDE.

In the Bayesian analysis, we first sample the RMF parameters [see Eq. (2)] from the prior distributions specified in Table 1. Using the RMF formalism outlined in Sec. II, we then generate the posterior distribution of the NMPs by applying constraints on the binding energies and charge radii of the $^{40}Ca_{20}$ and $^{208}Pb_{82}$ nuclei within 2% of their experimental values. For this purpose, we employ a Gaussian likelihood, defined as,

$$\log \mathcal{L}(\mu, \sigma_i^2 \mid \Theta) = -\frac{1}{2}\sum_{i=1}^{n}\left[\log\left(2\pi\sigma_i^2\right) + \frac{(\mu_i - y_i)^2}{\sigma_i^2}\right], \quad (12)$$

where μ_i are the experimental values of the FN observables, y_i are the corresponding RMF predictions, and σ_i are the associated uncertainties (taken as 2% of μ_i). We additionally generate another posterior distribution using the NML emulator to obtain the corresponding predictions.

Fig. 8 presents the posterior distributions of the NMPs obtained from the Bayesian analysis for both the NML and RMF models. The diagonal plots display the median and 68% CI of the marginal posterior distributions for the NMPs. The two-dimensional distributions and the one-dimensional marginalized posterior distributions shown along the diagonal are very similar for the RMF and NML cases. The comparatively broad posterior of Q_0 reflects the weaker sensitivity of the considered low-density FN properties, such as BE and R_{ch}, to this higher-order parameter, which becomes increasingly relevant at densities above saturation. We emphasize that this similarity demonstrates that the NML has successfully captured the underlying correlations of the RMF model while being explored over a wide parameter range. To provide a quantitative assessment, we calculate the JS divergence for the distributions of the individual NMPs, as indicated alongside the diagonal plots in Fig. 8. The good performance of NML is supported by these JS divergence values, all of which remain below 0.1. The pairwise correlations among the NMPs are also faithfully reproduced by NML in the Bayesian sampling, in close agreement with those obtained from the RMF model. Such correlations, as highlighted in previous studies[2, 17, 67], play a central role in constraining nuclear matter properties. The ability of NML to capture not only the individual distributions of NMPs but also their mutual correlations is therefore a key strength of the approach. Further improvements can be achieved by training on a broader and more diverse set of nuclei. The computational cost is also expected to scale more favorably as additional nuclei are incorporated into the Bayesian analysis, a direction we reserve for future work with updated NML models. By employing the NML model in place of the RMF solver, the Bayesian sampling time is reduced by approximately three orders of magnitude ($\sim 10^3$), decreasing the runtime from about 4.5 hours to roughly 15 seconds. For a single evaluation, the computation of FN properties for a given parameter set exhibits an even larger acceleration, with a speedup factor of approximately 1.1×10^3, reducing the evaluation time from about 2 seconds to 1.5 milliseconds. The RMF calculations used to construct the NML training dataset are performed offline and are not repeated during Bayesian sampling. Thus, the reported computational cost corresponds to the repeated likelihood evaluations during inference, for which the trained NML surrogate replaces the RMF solver. The specifications of the computing system and neural network architecture used in this study are detailed in Appendix A.

At this stage, it is worth reiterating the primary goal of the NML framework proposed here. When applied in a Bayesian analysis with explicit constraints from finite nuclei, the model is designed to explore wide parameter ranges while avoiding erroneous sampling of outliers. This flexibility also allows NML to be incorporated alongside complementary constraints from finite-nuclei studies [68] or astrophysical observations. It should also be emphasized that our objective is not to construct an extremely precise global mass model, a direction in which machine learning has already been extensively applied in nuclear physics[32−35, 69−77]. Rather, the purpose of NML is to enable large-scale Bayesian analyses that incorporate explicit finite-nuclei constraints into analyses of NS properties while remaining rooted in a microscopic description and retaining computational efficiency.

V. SUMMARY AND OUTLOOK

We employed a machine learning framework to develop an emulator of RMF theory with improved computational performance, enabling the efficient incorporation of explicit finite-nucleus constraints on the neutron star equation of state (EoS) [17]. A neural network model was trained using a large dataset generated from RMF theory calculations. The dataset includes binding energies and charge radii for several nuclei obtained for a large set of nuclear matter parameters (NMPs). The neural network architecture of NucleiML (NML) consists of a classifier and a regressor. The NML classifier determines whether the input parameters yield convergent finite-nucleus properties. The classifier achieved an accuracy of 95% in categorizing inputs into two classes: admissible and non-admissible. The NML regressor predicts the binding energies and charge radii for inputs classified as *admissible* by the classifier. The regressor achieved deviations in the binding energies and charge radii of less than ~ 5% for 95% of the test dataset, indicating sufficient accuracy for explicitly incorporating FN properties into a Bayesian analysis. The performance of the NML regressor on unseen nuclei improves significantly when the training set

CPC Accepted

includes more diverse nuclei, indicating the potential to extend the framework to larger and more diverse sets of nuclei.

The NML was incorporated into a Bayesian framework to constrain the NMPs based on FN experimental data. The results of the Bayesian analyses using NML closely matched those obtained with the RMF model. The Jensen-Shannon divergence values indicate high similarity between the marginalized posterior distributions for the NMPs considered with NML and the RMF model. NML also substantially accelerates computations compared with the RMF model, reducing the Bayesian sampling runtime from about 4.5 hours to roughly 15 seconds, corresponding to a speedup of approximately three orders of magnitude.

The NML demonstrates how machine learning can efficiently replicate the predictive capabilities of computationally intensive RMF models. The substantial reduction in computational time makes NML a highly efficient alternative while maintaining accuracy, facilitating faster exploration of the parameter space in Bayesian inference. It provides a promising approach for accelerating nuclear property calculations and enables more accessible integration of explicit FN and astrophysical constraints on the global behavior of the EoS into Bayesian frameworks for uncertainty quantification and parameter optimization. Moreover, the improved performance of the regressor with the inclusion of more diverse nuclei in the training set provides strong motivation to extend this work in that direction. Furthermore, incorporating deformed nuclei will provide a more stringent test of generalization at the mean-field level by enabling the emulator to learn features associated with collective deformation and long-range correlations beyond spherical systems. This framework can also be extended to other EDF families, such as Skyrme or Gogny, by generating consistent training datasets and redefining the corresponding input parameter spaces while retaining the same surrogate architecture. We leave these directions for future exploration.

ACKNOWLEDGMENTS

The authors gratefully acknowledge valuable suggestions and discussions with Prasanta Char. BKA gratefully acknowledges support received under the Raja Ramanna Chair scheme of the Department of Atomic Energy (DAE), Government of India.

DATA AVAILABILITY

The general architecture and additional details of the neural network are provided in Fig. 1 and in A. The training dataset and the weights of *NucleiML* will be made available upon request.

APPENDIX A: NEURAL NETWORK SPECIFICATIONS AND PERFORMANCE METRICS

We used an AMD EPYC 7452 32-core processor with an x86_64 architecture to train the neural networks. The processor operates at a base clock speed of 1.5 GHz and a boost clock speed of 2.35 GHz. This computational setup enabled efficient model training on a dataset containing approximately 1,000,000 samples. For classification tasks, the NucleiML classifier uses the Rectified Linear Unit (ReLU) activation function in the hidden layers, while the output layer uses a softmax activation function with a normal kernel initializer. For regression tasks, the NML regressors also use ReLU activation functions in the hidden layers, whereas the output layer uses a linear activation function. The classifier and regressors are trained using learning rates of 10^{-4} and 10^{-3}, respectively, with the Adam optimizer [78]. Hyperparameter tuning is performed via grid search, implemented using the Scikit-learn and SciKeras Python packages [61]. The key configurations are summarized as follows:

In addition to the hyperparameters discussed in Sec. IIIA, several others play an important role. The batch size specifies the number of training samples used before the model weights are updated. Larger batch sizes generally yield smoother training but may reduce generalization performance. For the NML framework, the optimal batch sizes were found to be 32 for the classifier and 128 for the regressor. Another class of hyperparameters controls fitting behavior through regularization techniques, such as dropout rates or weight decay, which are commonly used to prevent overfitting and improve generalization. However, in this study, the use of such regularization parameters resulted only in underfitting; therefore, they were not employed in the final analysis.

The dataset was partitioned into training, validation, and test sets at a 70:15:15 ratio for the classifier and a 70:21:9 ratio for the regressor, using a fixed random seed to ensure reproducibility. Hyperparameter tuning was performed using three-fold cross-validation on the training set, with model selection based exclusively on validation performance. Training was conducted for a minimum of 600 epochs for the classifier and 300 epochs for the regressor, with early stopping applied thereafter based on

CPU:	AMD EPYC 7452
Architecture:	x86_64
Cores:	32-cores, with 2 threads per core
Base Clock Speed:	1.5 GHz
Max. Clock speed:	2.35 GHz
Activation functions used:	ReLU (Classifier and Regressor)
	SoftMax (outer layer for Classifier)
	Linear (outer layer for Regressor)

CPC Accepted

validation loss to prevent overfitting while ensuring adequate convergence. Throughout this procedure, data subsets were carefully separated to prevent any form of data leakage, ensuring that neither validation nor test samples influenced model fitting or hyperparameter optimization.

Appendix B: The role of the classifier

Conceptual role

The NML framework uses the classifier as an admissibility filter that operates before the regressor. This design is motivated by the fact that not all sampled parameter sets correspond to physically meaningful or numerically converged RMF solutions. The regressor is trained to approximate RMF predictions over the admissible parameter space. However, admissibility is not intrinsically enforced within the regression framework; the classifier therefore fulfills this role.

The classifier partitions the parameter space into admissible and non-admissible regions. This separation ensures that the regressor operates only in admissible regions, where the mapping between the NMPs and FN observables is well defined and physically meaningful.

Representative examples

The non-admissibility of a given combination of NMPs arises from one of the following causes:

- **Non-convergent:** RMF results that fail to produce stable FN observables, even after 999 iterations.

- **No couplings generated:** Combinations of NMPs that do not yield reasonable coupling parameters.

- **Threshold check:** An FN observable deviates from the experimental observation by more than a specified threshold (20% in our case).

Table B1 presents a representative set of examples, along with the corresponding reasons for their classifications.

Effect on Posterior Distributions

To quantitatively assess the impact of the classifier on the Bayesian inference setup, posterior distributions were computed with and without the admissibility filter. The posterior distributions and median values of J_0 and L_0 (shown in Fig. B1) exhibit small but systematic shifts relative to those obtained with the RMF model. The corres-

CPC Accepted

Table B1. Representative RMF parameter sets illustrating the admissibility classification. Sets 1–3 are representative non-admissible parameter sets, whereas Sets 4–5 are representative admissible cases. The inputs to the NML consist of both the NMPs and the neutron and proton numbers (N,Z). The admissible examples therefore show results for two different nuclei, ^{208}Pb (Set 4) and ^{40}Ca (Set 5). The coupling constants are obtained from the inverse mapping described in Appendix D.

	Set 1	Set 2	Set 3	Set 4	Set 5
			NMPs		
r_0	0.1482	0.1616	0.1698	0.148	0.148
E_0	−15.789	−15.570	−16.086	−16.24	−16.28
K_0	205.889	299.820	226.976	271.53	229.54
Q_0	−1374.928	−1394.497	−644.027	202.91	−523.93
m_{eff}	0.581	0.765	0.736	0.60	0.61
J_0	20.326	38.108	39.218	37.4	32.56
L_0	29.328	90.025	55.929	118.53	60.44
			FN inputs		
N	–	20	8	126	20
Z	–	20	8	82	20
Flag	Non-admissible	Non-admissible	Non-admissible	Admissible	Admissible
Reason	No couplings generated	FN values not converged	FN values converged	–	–
BE (RMF)	–	–	−101.35	−1609.17	−354.38
BE (NML)	–	–	–	−1614.86	−353.81
R_{ch} (RMF)	–	–	2.33	5.50	3.41
R_{ch} (NML)	–	–	–	5.47	3.39
Iterations	–	999	506	–	–

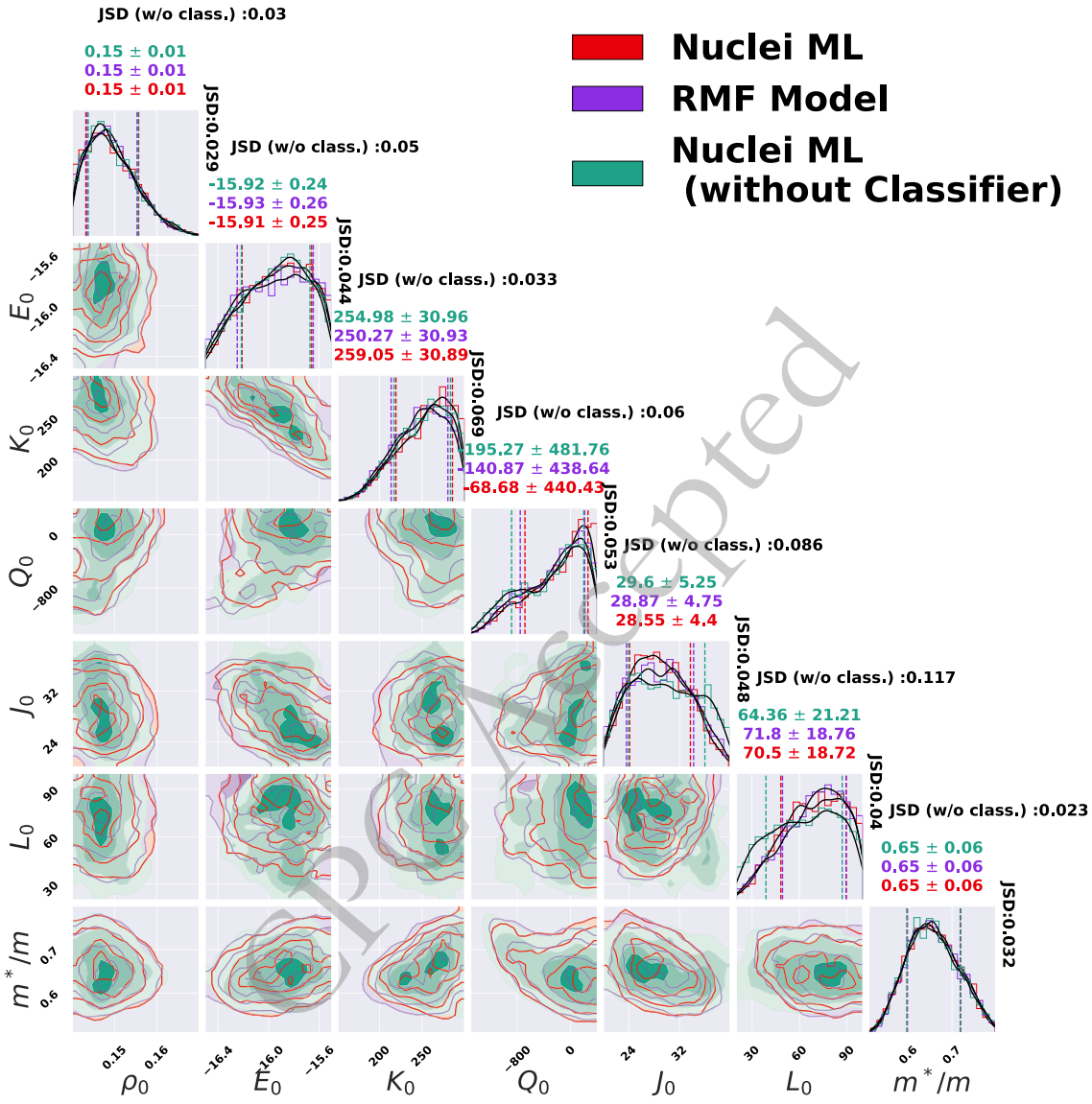


Fig. B1. (color online) Bayesian analysis using NucleiML (red), the RMF model (violet), and NucleiML without the classifier (green).

ponding JS divergence values quantify these differences and indicate a modest increase in divergence when the classifier is not used. The credible intervals for certain parameters, notably J_0 and L_0, are moderately broader without the classifier. Although the shifts observed without the classifier are moderate in magnitude and the credible intervals remain largely overlapping, they are systematic and measurably increase the JS divergence for certain parameters, particularly J_0 and L_0. Since NucleiML aims to serve as a faithful emulator of the underlying model, even such modest but reproducible deviations are undesirable. Including the classifier reduces these shifts and improves agreement with the posteriors obtained from the RMF model.

Threshold Sensitivity Analysis

The admissibility threshold, defined relative to experimental observables, determines the range within which a parameter set is considered admissible. Selecting this threshold involves a compromise between physical selectivity and numerical efficiency. An overly restrictive threshold may substantially narrow the admissible region, introduce class imbalance in the training dataset, and increase rejection rates during Bayesian sampling. Conversely, a permissive threshold may admit markedly unphysical parameter combinations, thereby reducing the physical interpretability of the posterior distributions. To assess the robustness of our chosen criterion (a 20% relative threshold), we performed a systematic sensitivity analysis by varying the admissibility condition. Specifically, classifier performance was evaluated for relative thresholds of 30%, 20% (reported in the main

CPC Accepted

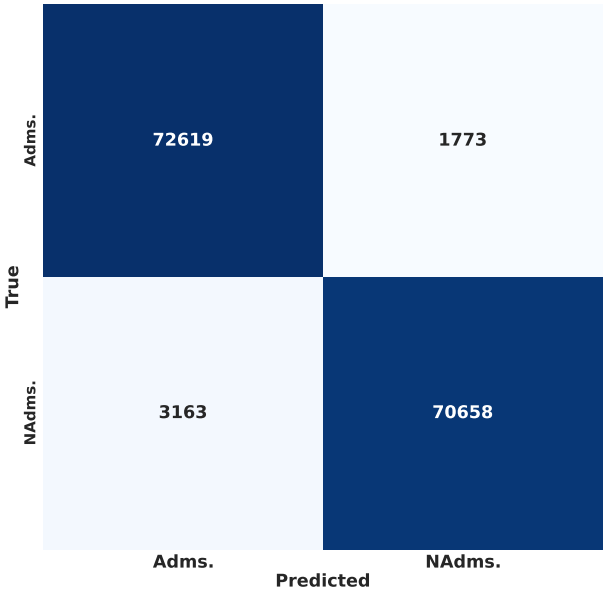


Fig. B2. (color online) Threshold of 30%

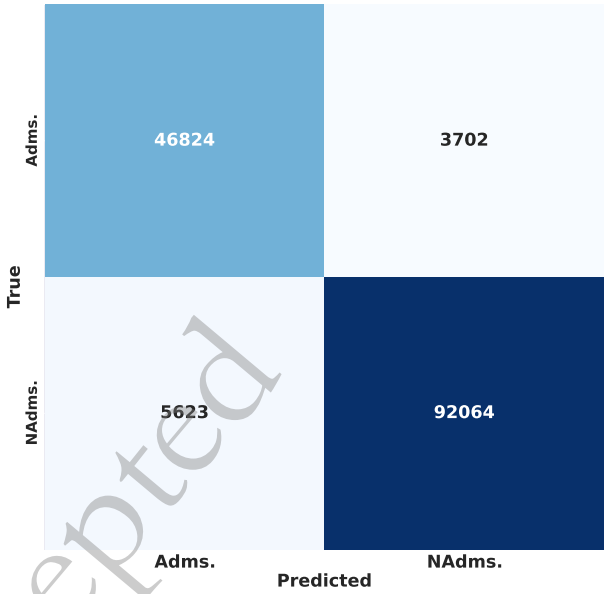


Fig. B4. (color online) Threshold of 10%

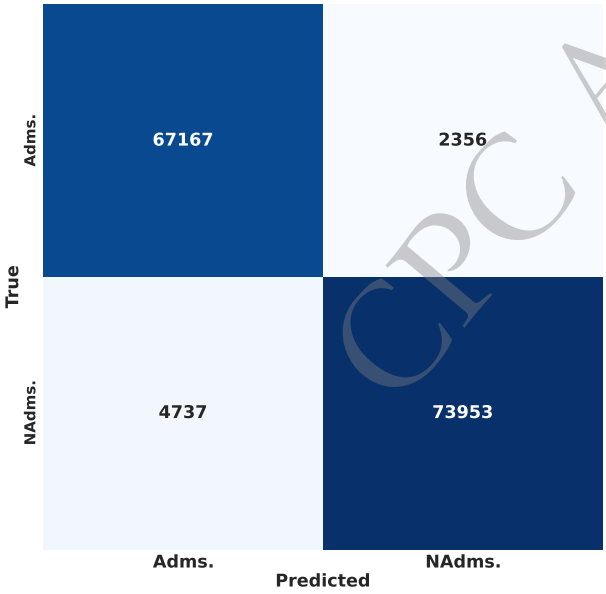


Fig. B3. (color online) A threshold of 20% is also reported in Fig. 3.

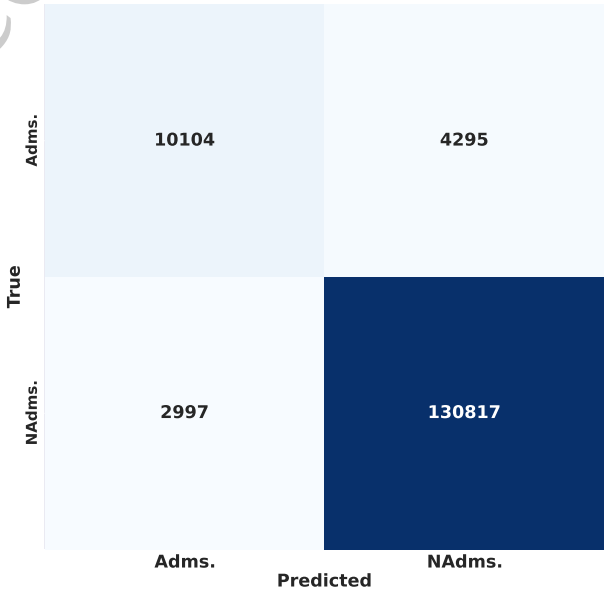


Fig. B5. (color online) A fixed threshold of 10 MeV was used across the nuclei.

CPC Accepted

manuscript), and 10%, as well as for a fixed absolute threshold of 10 MeV. The resulting accuracy, precision, and recall for both admissible and non-admissible classes are summarized in Table B2. The confusion matrices are shown in Fig. B6.

The overall classification accuracy remains high across all threshold choices, exceeding 93% in every case. For the relative thresholds (30%, 20%, and 10%), precision and recall gradually decrease as the criterion becomes more restrictive, reflecting the increasing difficulty of distinguishing admissible from non-admissible regions under tighter physical constraints. Notably, the 20% and 30% thresholds maintain a relatively balanced trade-off between precision and recall for both classes. In contrast, the fixed 10 MeV absolute threshold introduces a pronounced asymmetry in precision and recall. This behavior is primarily attributable to the strong class imbalance induced by the absolute admissibility criterion, which substantially reduces the number of admissible samples. Consequently, the classifier exhibits reduced recall for the admissible class while maintaining high recall for the non-admissible class.

Beyond classification metrics, the impact of threshold variation on Bayesian inference was also examined (see

Table B2. Sensitivity of classifier performance to the admissibility threshold.

Metric	30% (relative)	20% (relative)	10% (relative)	10 MeV (absolute)
Accuracy	0.9667	0.9521	0.9371	0.9508
Precision (admissible)	0.9583	0.9341	0.8928	0.7712
Recall (admissible)	0.9762	0.9661	0.9267	0.7017
Precision (Non-admissible)	0.9755	0.9691	0.9613	0.9682
Recall (Non-admissible)	0.9572	0.9398	0.9424	0.9776

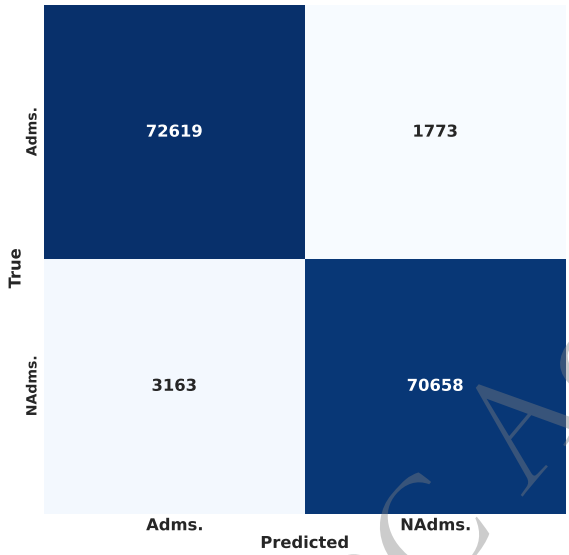


FIG. B2. Threshold of 30%

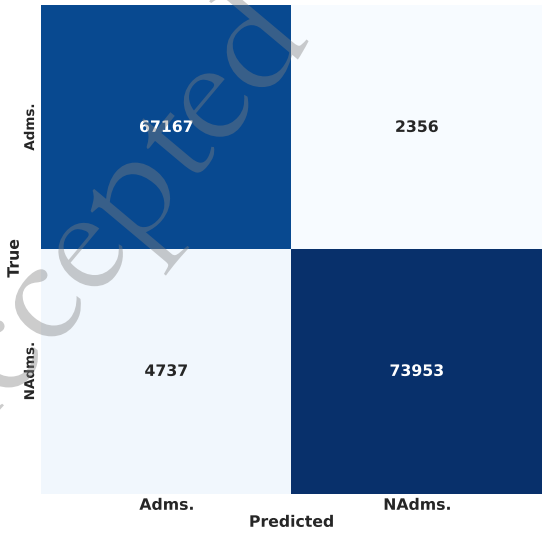


FIG. B3. A threshold of 20% is also reported in Fig.3.

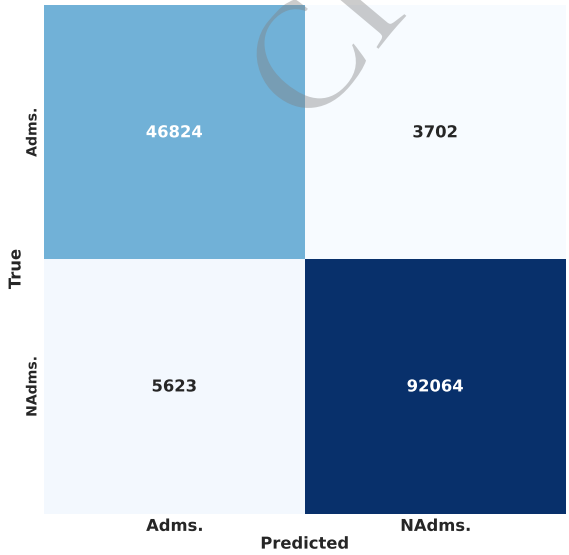


FIG. B4. Threshold of 10%

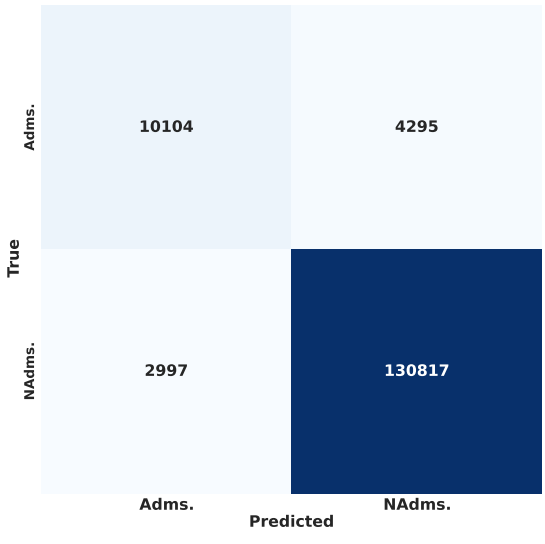


FIG. B5. A fixed threshold of 10 MeV was used across the nuclei.

Fig. B6. (color online) Confusion matrices showing classifier performance at different thresholds.

Fig. B7). The posterior distributions corresponding to each threshold remain statistically consistent, with no evidence of systematic bias or artificial concentration in parameter space. Although mild quantitative differences in spread are observed, the global structure of the inferred NMP distributions remains stable. This result indicates that the inference mechanism is robust to reasonable variations in the admissibility threshold.

CPC Accepted

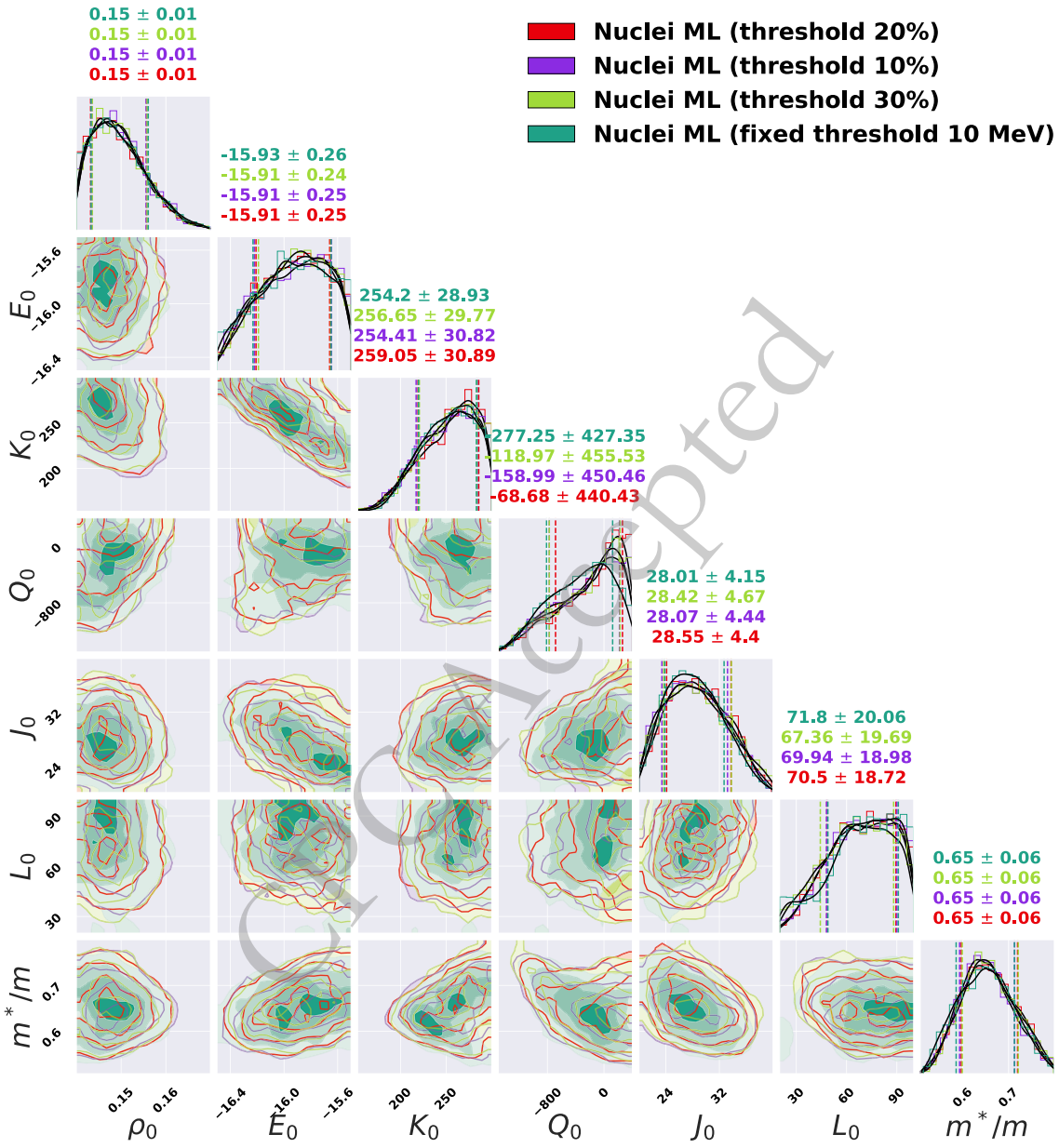


Fig. B7. (color online) The posterior distributions from the Bayesian analyses with different thresholds are presented. The median values for both cases are shown above the diagonal plots, which display the marginalized posterior distributions with the 68% CI indicated by vertical dashed lines.

Computational efficiency was also assessed. For the relative thresholds (30%, 20%, and 10%), sampling run times remain comparable (approximately 15–16 seconds). However, the absolute 10 MeV threshold nearly doubles the run time (approximately 30 seconds), reflecting the significantly narrowed admissible region and the corresponding increase in sampling rejection rates. Overall, this analysis demonstrates that relative thresholding preserves both physical interpretability and computational efficiency. Among the cases considered, the 20% relative criterion provides a conservative yet stable choice, yielding balanced classifier performance, robust posterior inference, and efficient Bayesian sampling.

APPENDIX C: PERFORMANCE BASED ON INDIVIDUAL NUCLEUS

Relative Error for Trained Nuclei

The figure shows the probability density distributions of the relative errors, $\Delta X/X$, for the binding energy (BE) and charge radius ($R_{\rm ch}$) of $^{40}Ca_{20}$ and $^{208}Pb_{82}$. In both panels, the distributions are sharply peaked near zero, indicating that the NML surrogate produces essentially un-

biased predictions. The dashed vertical lines denote the mean relative errors, and the legend reports the mean and standard deviation, with the value in parentheses indicating the 95% CI. For both nuclei, the charge-radius errors exhibit a noticeably narrower spread than the binding-energy errors, reflecting lower variance and greater stability in radius predictions. The heavier nucleus, $^{208}Pb_{82}$, shows slightly tighter distributions overall, suggesting improved robustness in the heavy-mass region. The consistently high R^2 scores in each panel further confirm the strong agreement between the surrogate predictions and the reference RMF calculations for these benchmark systems.

R^2 scores for unseen nuclei

Table C1 summarizes the generalization performance of the NML surrogate for unseen nuclei in terms of the coefficient of determination (R^2) for both binding energy and charge radius. The Initial Set exhibits limited predictive capability for several nuclei, with strongly negative R^2 values in some cases (e.g., $^{56}Ni_{28}$ and $^{100}Sn_{50}$ for binding energy), indicating poor generalization outside the training domain. Progressive augmentation of the training data (Initial + I and Initial + II) leads to a marked and systematic improvement in generalization accuracy, particularly for binding energies, for which most nuclei achieve positive and often high R^2 values under the Initial + II configuration. Improvements are also observed for charge radii, although the behavior is more nucleus-dependent and reflects the greater sensitivity of radius predictions to data coverage. Overall, the results demonstrate that targeted dataset enrichment substantially enhances the surrogate's robustness and stabilizes predictions in regions of parameter space not explicitly sampled during training.

APPENDIX D: MAPPING NUCLEAR-MATTER PARAMETERS TO RMF COUPLINGS

The nuclear-matter parameters (NMPs) are related to the RMF coupling parameters through the properties of uniform nuclear matter. Following Refs. [53, 54], we first construct the energy per particle and the symmetry energy as functions of the baryon density and the RMF couplings. The NMPs are then obtained from these quantities and their density derivatives evaluated at the saturation density.

In symmetric nuclear matter, the Fermi momentum is

CPC Accepted

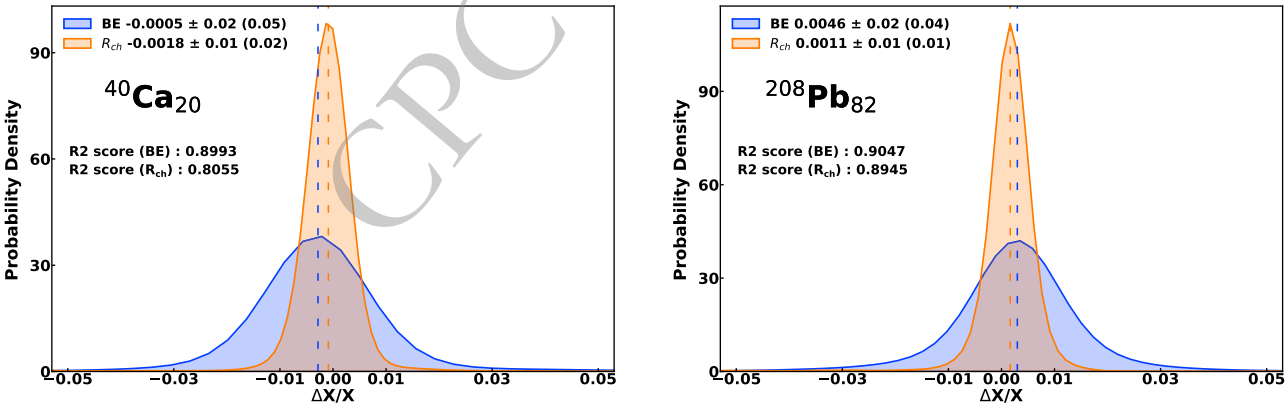


Fig. C1. (color online) Relative errors ($\Delta X/X$, Eq. 9) in the binding energies and charge radii of $^{40}Ca_{20}$ and $^{208}Pb_{82}$

Table C1. R^2 scores for binding energy and charge radius in unseen nuclei across different training configurations. Negative values indicate poor generalization performance.

Nucleus	Binding Energy (R^2)			Charge Radius (R^2)		
	Initial Set	Initial + I	Initial + II	Initial Set	Initial + I	Initial + II
$^{30}Ne_{10}$	0.1342	0.7662	0.6297	−0.2837	−0.6734	−3.0926
$^{54}Ca_{20}$	0.1871	0.8840	0.9005	0.6199	0.7072	0.6906
$^{56}Ni_{28}$	−1.8191	−0.3130	0.0242	0.7626	0.6407	−0.9842
$^{100}Sn_{50}$	−0.5571	−1.9090	0.0697	−0.3953	0.5338	0.3313
$^{116}Sn_{50}$	0.8300	0.5185	0.9019	0.4634	0.7097	0.9023
$^{138}Sn_{50}$	0.8410	0.8589	0.8442	0.7246	0.7155	0.6805
$^{144}Sm_{62}$	0.7209	0.5268	0.8239	0.3301	0.5170	0.5881

$$k_F = \left(\frac{3\pi^2\rho}{2}\right)^{1/3}, \tag{D1}$$

and the effective nucleon mass is

$$m^* = m - g_\sigma\sigma. \tag{D2}$$

The corresponding effective Fermi energy is

$$E_F^* = \sqrt{k_F^2 + m^{*2}}. \tag{D3}$$

The energy density of symmetric nuclear matter is

$$\varepsilon(\rho) = \frac{4}{(2\pi)^3}\int_0^{k_F} d^3k\ \sqrt{k^2+m^{*2}} + \frac{1}{2}m_\sigma^2\sigma^2 + \frac{A}{3}\sigma^3 + \frac{B}{4}\sigma^4 + \frac{1}{2}m_\omega^2\omega_0^2 + \frac{3}{4}Cg_\omega^4\omega_0^4, \tag{D4}$$

where the scalar and vector mean fields are determined self-consistently from

$$m_\sigma^2\sigma + A\sigma^2 + B\sigma^3 = g_\sigma\rho_s, \tag{D5}$$

$$m_\omega^2\omega_0 + Cg_\omega^4\omega_0^3 = g_\omega\rho, \tag{D6}$$

with the scalar density

$$\rho_s = \frac{4}{(2\pi)^3}\int_0^{k_F} d^3k\ \frac{m^*}{\sqrt{k^2+m^{*2}}}. \tag{D7}$$

Thus, the energy per particle, expressed relative to the free nucleon mass, is

$$E(\rho) = \frac{\varepsilon(\rho)}{\rho} - m. \tag{D8}$$

For asymmetric nuclear matter, the symmetry energy is defined using the expansion

$$E(\rho,\delta) = E(\rho,0) + S(\rho)\delta^2 + O(\delta^4), \qquad \delta = \frac{\rho_n-\rho_p}{\rho}. \tag{D9}$$

In the RMF model considered here, the symmetry energy is

$$S(\rho) = \frac{k_F^2}{6E_F^*} + \frac{g_\rho^2\rho}{8\left[m_\rho^2 + \Lambda_v g_\rho^2 g_\omega^2\omega_0^2\right]}. \tag{D10}$$

Thus, for a given set of RMF couplings

$$\boldsymbol{g} = \{g_\sigma, g_\omega, g_\rho, A, B, C, \Lambda_v\},$$

The functions $E(\rho)$ and $S(\rho)$ are obtained by solving the mean-field equations at each density. The NMPs at saturation density are then defined as

$$\rho_0: \quad \left.\frac{\partial E}{\partial\rho}\right|_{\rho_0} = 0, \tag{D11}$$

$$E_0 = E(\rho_0), \tag{D12}$$

$$K_0 = 9\rho_0^2\left.\frac{\partial^2 E}{\partial\rho^2}\right|_{\rho_0}, \tag{D13}$$

$$Q_0 = 27\rho_0^3\left.\frac{\partial^3 E}{\partial\rho^3}\right|_{\rho_0}, \tag{D14}$$

$$m^* = m - g_\sigma\sigma(\rho_0), \tag{D15}$$

$$J_0 = S(\rho_0), \tag{D16}$$

$$L_0 = 3\rho_0\left.\frac{\partial S}{\partial\rho}\right|_{\rho_0}. \tag{D17}$$

Equivalently, the saturation condition may be written as

$$P_0 = \rho_0^2\left.\frac{\partial E}{\partial\rho}\right|_{\rho_0} = 0. \tag{D18}$$

In this study, the seven sampled NMPs

$$\boldsymbol{p} = \{\rho_0, E_0, K_0, Q_0, m^*/m, J_0, L_0\}$$

are mapped onto the seven RMF coupling parameters

$$\boldsymbol{g} = \{g_\sigma, g_\omega, g_\rho, A, B, C, \Lambda_v\}.$$

For each sampled $\boldsymbol{p}$, the equations above define a seven-dimensional nonlinear system whose solution yields

CPC Accepted

Table D1. Representative RMF coupling parameters corresponding to the parameter sets listed in Table B1. The coupling parameters follow the convention of the Lagrangian in Eq. (1). The nonlinear scalar coupling A is given in units of fm^{-1}, while B, C, and Λ_v are dimensionless. Set 1 does not yield a valid set of RMF couplings. Sets 2–5 are representative samples obtained from the inverse NMP-to-coupling mapping described in Appendix D.

Set	g_σ	g_ω	g_ρ	A	B	C	Λ_v
Set 1	–	–	–	–	–	–	–
Set 2	7.49021	9.44645	9.96381	−16.5260	163.123	0.0395807	0.0360820
Set 3	8.26880	9.39336	11.9625	15.2052	−3.81461	0.00749072	0.0913851
Set 4	10.4238	14.3417	9.29092	8.31892	4.49613	0.00524374	−0.000889487
Set 5	10.9721	14.3348	11.7883	4.70253	57.7092	0.0100119	0.0598579

the corresponding coupling parameters. The density derivatives appearing in K_0 and L_0 are evaluated using a centered finite difference with $h = 10^{-6}$.

The resulting seven-dimensional nonlinear system is solved using the `fsolve` routine of SciPy, which employs the Powell hybrid method when no Jacobian is supplied. The coupling parameters of the FSUGold2 RMF parameterization serve as a fixed initial guess.

No additional parameter scaling is applied. We use the default `fsolve` convergence tolerance, $\mathrm{xtol} = 1.49012 \times 10^{-8}$; for the seven-dimensional system, the default maximum number of function evaluations is $100(N+1) = 800$. The resulting coupling parameters are listed in Table D1.

We do not assume that the inverse mapping from NMPs to RMF couplings is globally unique. The current implementation selects the solution obtained from the specified initial guess and consistently uses this branch when constructing the NucleiML dataset.

CPC Accepted

References

[1] Tsang C Y, Tsang M B, Danielewicz P *et al.* 2020 *Phys. Rev. C* **102**(4) 04808 ISSN 24699993
[2] Patra N K, Venneti A, Imam S M A *et al.* 2023 *Phys. Rev. C* **107**(5) 055804 ISSN 2469-9985
[3] Wang M, Huang W, Kondev F *et al.*, Chin. Phys. C **45**, 030003 (2021)
[4] Angeli I and Marinova K P, At. Data Nucl. Data **99**, 69 (2013)
[5] Dutra M, Lourenço O, Martins S *et al.*, Phys. Rev. C **85**(3), 035201 (2012)
[6] Tsang C Y, Tsang M B, Lynch W G *et al.*, Nat. Astron. **8**, 328 (2024)
[7] Fonseca E, Cromartie H T, Pennucci T T *et al.*, Astrophys. J. Lett. **915**, L12 (2021)
[8] Reardon D J, Bailes M, Shannon R M *et al.*, Astrophys. J Lett. **971**, L18 (2024)
[9] Riley T E, Watts A L, Bogdanov S *et al.*, Astrophys. J. Lett. **887**, L21 (2019)
[10] Riley T E, Watts A L, Ray P S *et al.*, Astrophys. J. Lett. **918**, L27 (2021)
[11] Miller M, Lamb F K, Dittmann A *et al.*, Astrophys. J. Lett. **887**, L24 (2019)
[12] Miller M C, Lamb F K, Dittmann A *et al.*, Astrophys. J. Lett. **918**, L28 (2021)
[13] Abbott B P, Abbott R, Abbott T *et al.*, Phys. Rev. Lett. **121**, 161101 (2018)
[14] Tsang M B, Zhang Y, Danielewicz P *et al.* 2009 *Phys. Rev. Lett.* **102**(12) 122701 ISSN 00319007
[15] Morfouace P, Tsang C Y, Zhang Y *et al.* 2019 *Phys. Lett. B* **799** 135045 ISSN 03702693
[16] Estee J, Lynch W G, Tsang C Y *et al.* 2021 *Phys. Rev. Lett.* **126**(16) 162701 ISSN 10797114
[17] Venneti A, Gautam S, Banik S *et al.*, Phys. Lett. B 138756 (2024)
[18] Gambhir Y and Ring P, Pramana **32**, 389 (1989)
[19] Gambhir Y K, Ring P and Thimet A 1990 *Ann. Phys.* **198**(1) 132 ISSN 1096035X
[20] Ring P, Gambhir Y and Lalazissis G 1997 *Comp. Phys. Comm.* **105** 77 ISSN 0010-4655
[21] Dax M, Green S R, Gair J *et al.*, Nat. **639**, 49 (2025)
[22] Abylkairov Y S, Edwards M C, Orel D *et al.*, Mach. Learn.: Sci. & Tech. **5**, 045077 (2025)
[23] Mitra A, Orel D, Abylkairov Y S *et al.*, Mon. Not. Roy. Astron. Soc. **529**, 3582 (2024)
[24] Manchanda A, Dainotti M G, Deepu A *et al.* 2024 (*Preprint* 2412.20091)
[25] Dainotti M G, De Simone B, Narendra A *et al.* 2025 (*Preprint* 2501.13102)
[26] Papigkiotis G and Pappas G, Phys. Rev. D **107**, 103050 (2023)
[27] Papigkiotis G, Vardakas G, Likas A *et al.* 2025 (*Preprint* 2501.18544)
[28] Thakur P, Malik T and Jha T K, Part. **7**, 80 (2024)
[29] Gonçalves G, Ferreira M, Aveiro J *et al.*, J. Cosmol. Astropart. Phys. **2023**, 001 (2023)
[30] Hatfield P W, Gaffney J A, Anderson G J *et al.*, Nat. **593**, 351 (2021)
[31] Benelli G, Chen T Y, Duarte J *et al.* 2022 *arXiv preprint arXiv: 2207.09060*
[32] Dellen B, Jaekel U, Freitas P S *et al.*, Phys. Lett. B **852**, 138608 (2024)
[33] Mumpower M, Li M, Sprouse T M *et al.*, Front. Phys. **11**, 1198572 (2023)
[34] Wu X, Ren Z and Zhao P 2024 *arXiv preprint arXiv: 2412.20739*

[35] Yüksel E, Soydaner D and Bahtiyar H, Phys. Rev. C **109**, 064322 (2024)
[36] Yang Z X, Fan X H, Li Z P *et al*., Phys. Rev. C **109**, 064312 (2024)
[37] Hizawa N, Hagino K and Yoshida K, Phys. Rev. C **108**, 034311 (2023)
[38] Munoz J M, Udrescu S M and Ruiz R F G 2024 *arXiv preprint arXiv: 2404.11477*
[39] Bollapragada R, Menickelly M, Nazarewicz W *et al*., J. Phys. G **48**, 024001 (2020)
[40] Giuliani P, Godbey K, Kejzlar V *et al*., Phys. Rev. Res. **6**, 033266 (2024)
[41] Ferreira M and Providência C, J. Cosmol. Astropart. Phys. **2021**, 011 (2021)
[42] Fujimoto Y, Fukushima K, Kamata S *et al*., Phys. Rev. D **110**, 034035 (2024)
[43] Jiang W G, Forssén C, Djärv T and Hagen G, Phys. Rev. C **109**(6), 064314 (2024)
[44] Svensson I, Tichai A, Hebeler K *et al*., Phys. Rev. C **113**(2), 024303 (2026)
[45] He W, Li Q, Ma Y *et al*., Science China Physics, Mechanics & Astronomy **66**, 282001 (2023)
[46] Goriely S, Choplin A, Ryssens W *et al*. 2023 *J Phys. Conf. Ser.* vol 2586 (IOP Publishing) p 012104
[47] Patra N, Malik T, Pais H *et al*., Physics Letters B **865**, 139470 (2025)
[48] Giuliani P, Godbey K, Bonilla E, Viens F *et al*. 2023 *Frontiers in Physics* **10**
[49] Bonilla E, Giuliani P, Godbey K *et al*., Phys. Rev. C **106**(5), 054322 (2022)
[50] McDonnell J D, Schunck N, Higdon D *et al*., Phys. Rev. Lett. **114**(12), 122501 (2015)
[51] Higdon D, McDonnell J D, Schunck N *et al*., Journal of Physics G: Nuclear and Particle Physics **42**, 034009 (2015)
[52] Belley A, Munoz J M and Garcia Ruiz R F, Phys. Rev. Lett. **136**(8), 082501 (2026)
[53] Dutra M, Lourenço O, Avancini S S *et al*., Phys. Rev. C **90**(5), 055203 (2014)
[54] Zhu Z, Li A and Liu T, Astrophys. J. **943**, 163 (2023)
[55] Nikšić T, Paar N, Vretenar D *et al*., Computer physics communications **185**, 1808 (2014)
[56] Danielewicz P, Lacey R and Lynch W G, Science **298**, 1592 (2002)
[57] Fèvre A L, Leifels Y, Reisdorf W *et al*. 2016 *Nucl. Phys. A* **945** 112 ISSN 03759474
[58] Lynch W G and Tsang M B 2022 *Phys. Lett. B* **830** 137098 ISSN 03702693
[59] Abadi M, Agarwal A, Barham P *et al*. 2015 TensorFlow: Large-scale machine learning on heterogeneous systems software available from tensorflow.org URL https://www.tensorflow.org/
[60] Chollet F *et al*. 2015 Keras https://keras.io
[61] Pedregosa F, Varoquaux G, Gramfort A *et al*., Journal of Machine Learning Research **12**, 2825 (2011)
[62] Mao A, Mohri M and Zhong Y 2023 *International conference on Machine learning* (PMLR) p 23803
[63] De Myttenaere A, Golden B, Le Grand B *et al*., Neurocomputing **192**, 38 (2016)
[64] Lin J 1991 *IEEE Transactions on Information Theory* **37**
[65] Kullback S and Leibler R A 1951 *Ann. Math. Stat.* **22** 79 ISSN 00034851
[66] MacKay D J 2003 (Cambridge university press)
[67] Malik T, Agrawal B K, Providência C *et al*., Phys. Rev. C **102**(5), 052801 (2020)
[68] Mondal C and Gulminelli F, Phys. Rev. C **107**, 015801 (2023)
[69] Neufcourt L, Cao Y, Nazarewicz W *et al*., Phys. rev. lett. **122**, 062502 (2019)
[70] Anil M U, Banerjee K, Malik T *et al*., J. Cosmol. Astropart. Phys. **2022**, 045 (2022)
[71] Wu X, Guo L and Zhao P, Phys. Lett. B **819**, 136387 (2021)
[72] Gao Z P, Wang Y J, Lü H L *et al*., Nuc. Sci. Tech. **32**, 109 (2021)
[73] Shelley M and Pastore A, Uni. **7**, 131 (2021)
[74] Niu Z and Liang H, Phys. Rev. C **106**, L021303 (2022)
[75] Mumpower M, Sprouse T, Lovell A *et al*., Phys. Rev. C **106**, L021301 (2022)
[76] Lovell A E, Mohan A T, Sprouse T M *et al*., Phys. Rev. C **106**, 014305 (2022)
[77] Li M, Sprouse T M, Meyer B S *et al*., Phys. Lett. B **848**, 138385 (2024)
[78] Kingma D P and Ba J 2014 *arXiv preprint arXiv: 1412.6980*

CPC Accepted